Noncontact radial pulse waveform acquisition system to estimate heart rate and radial augmentation index

Xunzhe Wen

Electrical and Computer Engineering

University of Ottawa

Ottawa, Canada

Purpose:

To develop a non-contact and non-invasive pulse waveform acquisition device using laser speckle imaging technique to measure heart rate and radial augmentation index.

Methods:

a. A literature review related to the topic was conducted.

b. The mathematic models was studied to reveal the relationship between skin deformation and pulse pressure waveform.

c. A prototype with hardware configuration and software design was developed

Mathematical Model Studies

The models which reveals the relationship between arterial blood pressure waveform and skin displacement have been studied by many investigators over many years.

In this chapter, it presents both models of arterial radial displacement and arterial wall mechanics, and the laser imaging principles have been also presented.

Hemodynamic Properties

The arterial radial displacement model established the relationship between radial displacement of the artery and blood pressure difference. The arterial wall model and skin tissue viscoelastic model studied the elastic and viscous mechanisms of the human tissue.

Based on the established models, we then draw conclusions that radial pulse pressure waveform could be detected as a form of skin displacement profile.

Arterial radial displacement model

In fluid dynamics, the blood flow can be calculated using the following equation:

$$F = \frac{\Delta P \pi r^4}{8vL} \quad (8)$$

where ΔP is the pressure difference along a given vessel, r is the radius of the vessel tube, v is the fluid viscosity, and L is the length of that vessel. Commonly, two mathematical models are used to model radial changes in a blood vessel [62].

Navier-Stokes Model

The first model is based on Navier-Stokes equations, and, it is given by:

$$-\frac{dP}{dx} = \rho \left(\frac{dw}{dt} + u\frac{dw}{dr} + w\frac{dw}{dr} \right) - \eta \left(\frac{d^2w}{dr} + \frac{1}{r}\frac{dw}{dr} + \frac{d^2w}{dx^2} \right) \quad (9)$$

2

$$-\frac{dP}{dr} = \rho\left(\frac{du}{dt} + \mu\frac{du}{dr} + w\frac{du}{dx}\right) - \eta\left(\frac{d^2u}{dr^2} + \frac{1}{r}\frac{du}{dx^2} + \frac{d^2u}{dx^2} + \frac{u}{r^2}\right) \quad (10)$$

where P is the pressure along the radial r and longitudinal x axes, w is the longitudinal velocity of the fluid in the longitudinal x direction, and u is the radial velocity of the fluid in the r direction. Fluid viscosity is denoted by η and density is denoted by ρ. In the equation (9) and (10), the mathematical terms in the first parentheses represent inertial forces, and the terms in the second parentheses represent viscous forces. Thus, difference between the inertial forces and the viscous losses equals a pressure drop per unit length. There is no general solution presented to Navier-Stokes equations; however, analytic solutions have been calculated for longitudinal flow velocity and longitudinal volume flow in an elastic tube under certain assumptions [63].

The velocity of the radial expansion of the vessel v, can be derived from the Navier-Stokes equations, as presented by Milnor [63]:

$$v = rC\frac{\Delta P}{dt} \quad (11)$$

where v is the radial velocity, r is the radius of the vessel in diastole, C describes the elastic properties of the arterial wall, and ΔP is the change in the blood pressure. If the blood pressure and the radial velocity of the arterial wall are given, the blood pressure change can be derived. By integrating Equation (11) with respect to time, the displacement profile can be derived as the Equation (12):

$$dr = rC \cdot \Delta P \quad (12)$$

Therefore, radial displacement dr of the blood vessel linearly depends on the blood pressure difference.

Bernoulli's law Model

Another model has been established based on Bernoulli's law. For the incompressible flow equation, Bernoulli's law is given as the following form:

$$\frac{1}{2}\rho v^2 + \rho gz + P = C \quad (13)$$

where ρ denotes the density of the fluid, v denotes the flow speed at a point on a streamline, g is

3

the gravitational acceleration, z denotes the elevation of the point above a reference plan, P is the pressure at that point, and C is an arbitrary constant [64]. The constant parameters on the right-hand side, v, z, P, depend on the particular point on the streamline. The first term in Equation (13) represents fluid dynamic pressure, while the second term denotes static pressure due to elevation of the fluid. The total pressure, which is the sum of the dynamic and static pressure in Bernoulli's equation, equals to a constant value. When blood flows in a vessel, pressure variations are generated in the direction of the blood flow. These pressure variations cause a force F that can be represented as:

$$F = -AdP \quad (14)$$

where A is the contact unit area of the arterial vessel, and dP is a change in blood pressure. The direction of force F is perpendicular to the cross section of the vessel. By introducing the Newton second law, Equation (14) can be rewritten in the following way:

$$-A\frac{dP}{dx}dx = \frac{dv}{dt}\rho A dx \quad (15)$$

where v is a longitudinal velocity. Equation (15) can be also written as the following way:

$$\frac{dP}{dx} = \rho\frac{dv}{dt} \quad (16)$$

In order to extract the relative radial displacement, Streeter used the same hypotheses as were considered in Milnor's Navier-Stokes solution and proposed a possible solution [65]. Thus, the relative radial displacement dr of a vessel is derived by:

$$dr \approx \frac{r}{E}dP \quad (17)$$

where r is the radius of the vessel in diastole, and E denotes the elastic modulus of the vessel wall, which is individual independent. From Equation (17), the relative radial displacement of a vessel is linearly dependent on the pressure difference in this vessel.
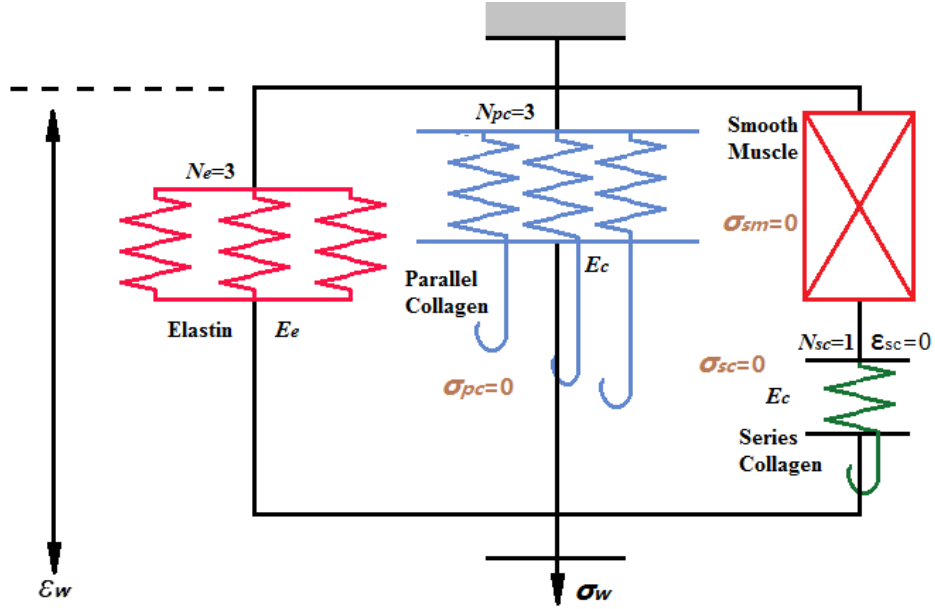

Arterial wall model

The structure of the arterial wall and the mechanism of its components are well studied [66, 67, 68, 69, 70]. In respect to anatomy, the arterial wall consists of four major components:

endothelium, elastin, collagen, and smooth muscle. Endothelium is in a form of cell layer, provides a smooth wall for blood flow and releases local chemicals to help regulate smooth muscle contraction. However, it contributes little to arterial wall mechanics. Elastin is much extensible and the abundant elastic fibers in arteries allow them to expand when blood pumped from the ventricles passes through them, and then recoil after the surge of blood has passed. Collagen is the ubiquitous reinforcing and load-bearing elements in arterial wall [71]. The organization and arrangement of collagen fibers maintains the integrity, strength, and function of arteries. Collagen is much stiffer than elastin, and does not exert tension until the arterial wall is stretched. From the previous scientific evidences, elastin plays a dominant role in arterial elasticity at low BP, while collagen markedly contributes to the arterial elasticity at high BP. Contracted smooth muscle via physiologic regulation or medication can modulate arterial elasticity. Note that except elastic, it makes the arterial wall viscous as well.

Different types of blood vessels share the same general components, but vary slightly in their structures and compositions. Elastin fibers are more abundant in the central arteries, which are named as elastic arteries, while smooth muscle is more prevalent in the peripheral arteries hence they are known as muscular arteries. Elementary mechanical components are considered as elastic or viscous, and some combination of both kinds is needed to simulate viscoelastic properties. In this paper, it will first discuss elastic properties of the artery and then consider its viscoelastic properties. Although there are some differences in material behaviors between elastic and viscoelastic, such as timeliness, deformation properties and material breakages, both of them are able to describe anti-deformation and deformation recovery of the material.

Elastic properties

The classic description to obtain viscoelastic constitutive models is using the mechanical analogs. These are simple mechanical models for fluid and solid representations that are put together to produce viscoelastic effects, for example, three standard mechanical models to express viscoelastic properties: Maxwell model, Voigt model, and St. Venant model. Commonly, springs represent purely elastic, and dashpots represent purely viscous. A Maxwell-type model has been employed from the literature to illustrate the elastic properties of the general arterial walls [72, 73].
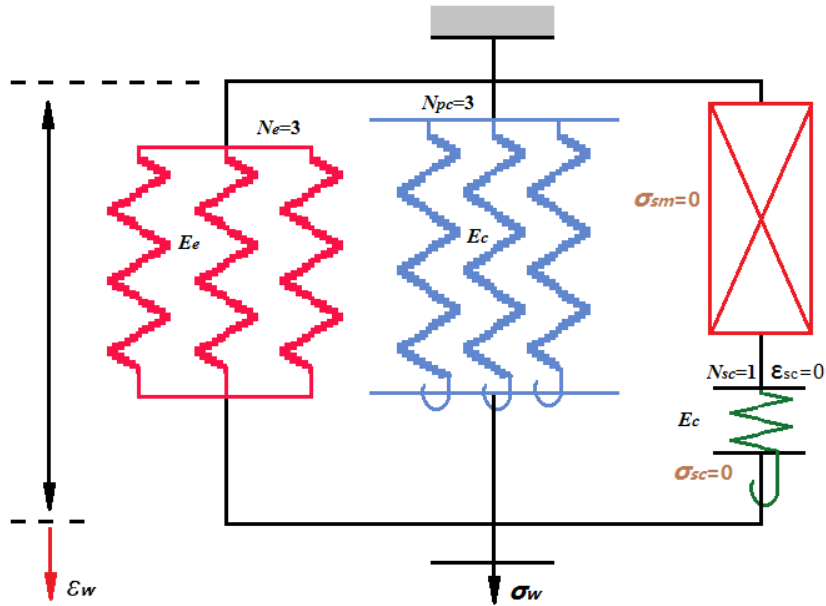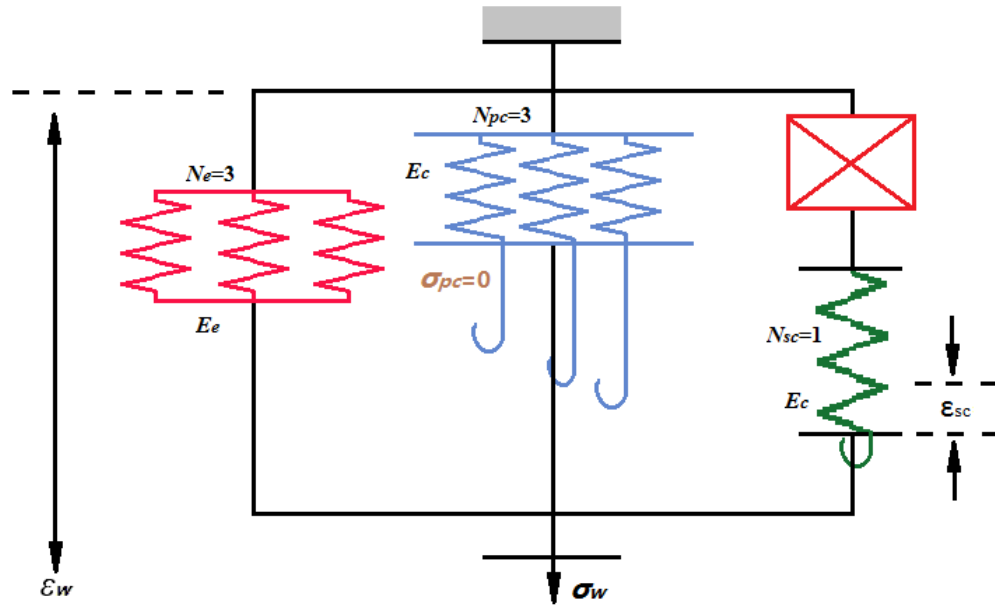
Figure 1. Model of the central arterial wall during smooth muscle relaxation. (a) shows that in the low extension state, (b) shows that in the high extension state.

Elastin is modeled by using a number of N_e springs, and each springs equips an elastic modulus E_e. Collagen is represented with a disconnecting hook model in which springs are recruited as the wall extends (parallel collagen) or as smooth muscle contracts (series collagen). The elastic

modulus of collagen denotes as E_c, which is defined 400 times larger than E_c, and the elastic modulus of parallel and series collagen is E_c respectively times the number of recruited fibers N_{pc} and N_{sc}. As the literature indicated, series collagen is recruited more easily than parallel collagen [73]. Smooth muscle is supposed to tolerate no stress and extend freely during relaxation and recruit the series collagen while the stress applied during contraction [74]. A strain generator in series with an elastic modulus varying spring, which denotes as VE_{sm}, is employed to model smooth muscle. During relaxation, there is no strain generated on the series collagen, and VE_{sm} is small, hence the smooth muscle extends freely. During contraction, strain is generated on the series collagen and VE_{sm} becomes large, thus series collagen determines the elasticity under this circumstances. In brief, smooth muscle contraction results in an increasing on both VE_{sm} and strain generation.

During smooth muscle relaxation, the strain generated on the series collagen ε_{sc} is zero, so none of these collagen fibers are recruited. In a low-extension case, as Figure 10(a) shows, the wall stress σ_ω and strain ε_ω will increase but not enough to recruit any parallel collagen. Hence the incremental elastic modulus E_{inc} of the arterial wall is determined only by elastin in this hypotensive state. In contrast, the wall stress σ_ω and strain ε_ω will remarkably increase, so that all of the parallel collagen can be recruited in this high-extension state, as Figure 10(b) shows. Thus, both parallel collagen and elastin contribute in this hypertensive state and E_{inc} increases accordingly.

Figure 11(a) and (b) respectively shows the model in the hypotensive and hypertensive states during smooth muscle contraction. Strain on the series collagen ε_ω increases so that all of the series collagen will be recruited. It's necessary to mention that ε_ω will decrease to maintain σ_ω due to the isotonic conditions, but not as much as ε_{sc} increases. There is no parallel collagen recruited as Figure 11(a) shows, so both elastin and series collagen determine the E_{inc} under the low-extension circumstance. Under the high-extension circumstance, some parallel collagen is recruited, and all components, which are parallel, series collagen and elastin, contribute the increasing in E_{inc}, as Figure 11(b) represents.
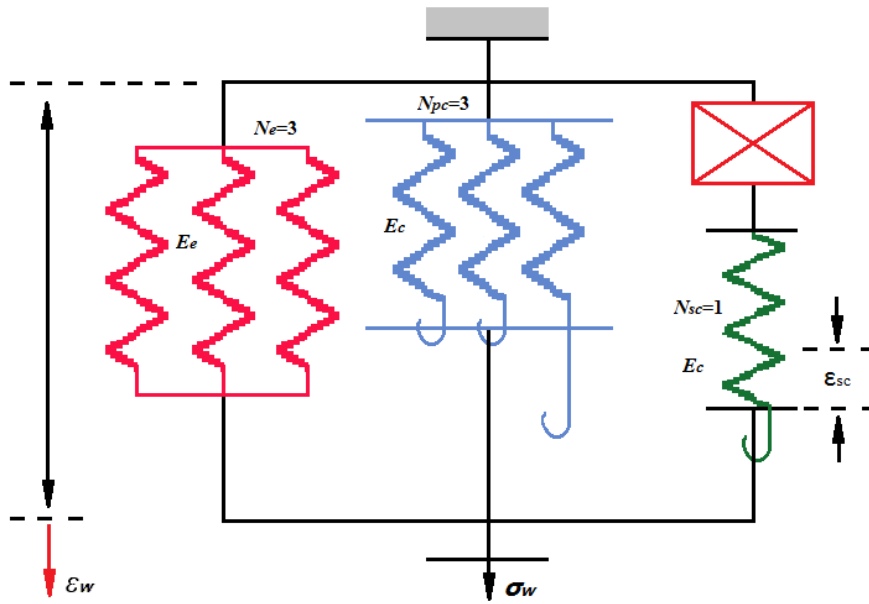
Figure 2. Model of the central arterial wall during smooth muscle contraction. (a) shows that in the low extension state, (b) shows that in the high extension state.

If consider this model in the central arteries, E_{inc} and ε_ω will not vary much compared to the corresponding circumstances during smooth muscle relaxation. Because N_{sc} is not that large and central arteries are relatively sparse in smooth muscle. Moreover, the reduction in ε_ω will result in a decrease in N_{pc} under the high-extension circumstance, which fully compensates the increase in N_{sc}. Compared to the previous described central arterial wall model, N_e is smaller while N_{sc} is much larger in the peripheral arterial wall because of the different compositions.
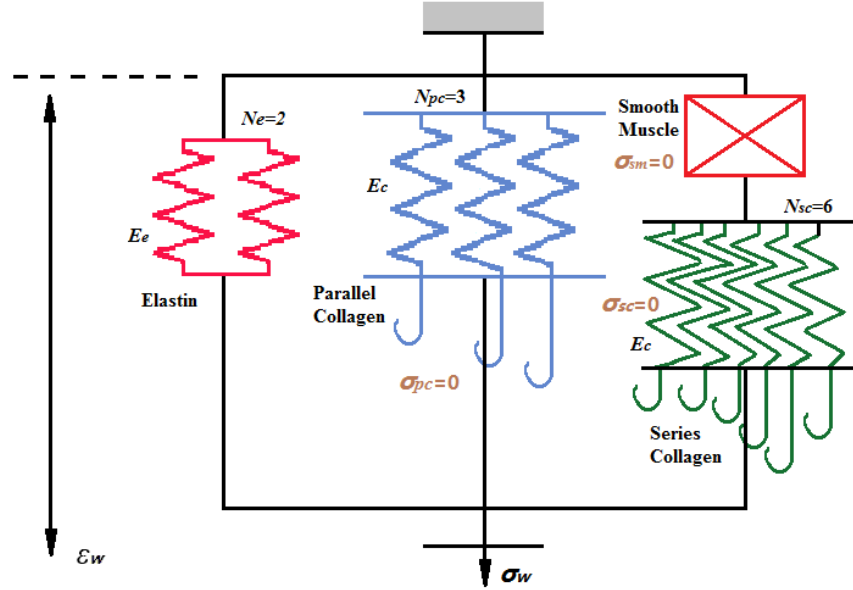

Figure 3. Model of the peripheral arterial wall in low-extension state during smooth muscle relaxation.

Figure 12 represents the peripheral arterial wall model, in which the number of springs and hooks represents relative amounts and the number of hooks indicates triggered rather than total fibers. During smooth muscle relaxation, E_{inc} in the peripheral arterial model are relatively smaller compared to the central arterial wall model in the hypotensive case, but similar in the hypertensive state. During smooth muscle contraction, E_{inc} and ε_ω will increase and decrease to a remarkable degree respectively, because of a larger amount of N_{sc}. Moreover, N_{pc} is smaller than N_{sc} so that the increase in N_{sc} cannot be entirely compensated by the decrease in N_{pc} under the high-extension circumstances.

In conclusion, elasticity in central arteries is influenced by BP but not smooth muscle contraction, and peripheral arterial elasticity is determined by both BP and smooth muscle contraction. Cox's work shows exemplary experimental data indicating that pressure–diameter relationships of both a central artery (thoracic aorta) and a peripheral artery (renal artery). Pressure-diameter relationship

are indeed similar in the relaxed and contracted states for a central artery, and different in that for a peripheral artery [74].

Viscous properties

A viscosity was employed into the arterial wall models to form unified viscoelastic models for arteries. The hypothesis of viscoelastic models originated from a review [75], which is based on vitro animal studies, in vivo animal studies, and an in vitro human studies [76, 77, 78, 79].

Viscosity is introduced in the smooth muscle model by using a parallel connected dashpot with the spring as Figure 13 shows, and the variable viscosity is denotes as $V_{\eta sm}$. While smooth muscle is relaxed, $V_{\eta sm}$ is small so that the arterial wall performs purely elastic, and $V_{\eta sm}$ is large so that the arterial wall is viscoelastic during contraction. In other word, $V_{\eta sm}$ will increase with smooth muscle contraction.
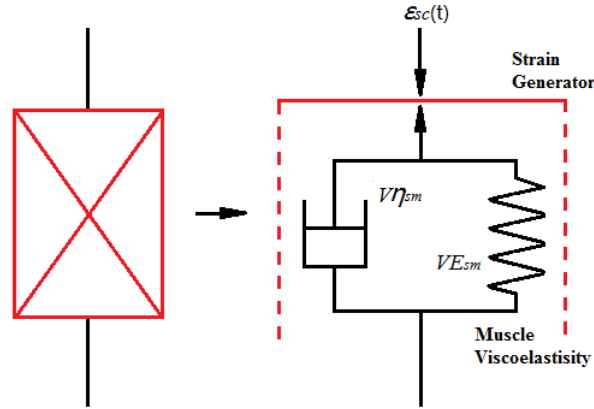

Figure 4. Viscoelastic model of smooth muscle.

A complete viscoelastic model of arterial wall for a fixed smooth muscle contraction and small changes in ε_ω is presented in Figure 14. The number of recruited collagen fibers will remain constant even though small variations in ε_ω. When apply a step increase in ε_ω, the stress will be immediately sustained by elastin and all recruited collagen fibers. Then the dashpot will gradually elongate until the stress is equally borne by the smooth muscle and series collagen, and the stress will decrease to a nonzero value with a time constant which is governed by these two components.

According to this viscoelastic model of artery, the elastic modulus as a function of frequency can be derived. The elastic modulus at low-frequency is presented as following equation:

$$E_{low} = E_{e-pc} + \frac{E_{sc} \cdot E_{sm}}{E_{sc} + E_{sm}} \quad (18)$$

while the elastic modulus at high frequency is represented:

$$E_{high} = E_{e-pc} + E_{sc} \quad (19)$$

In the central arterial wall model, the elastic modulus does not vary significantly with frequency due to the small value of E_{sc}. But E_{sc} is large in the peripheral arterial wall model so that the elastic modulus is of great dependence of frequency.
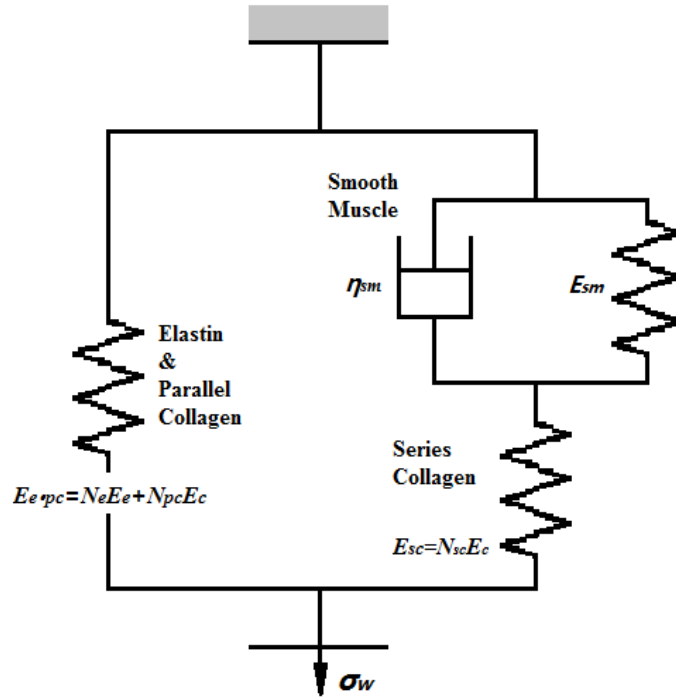

Figure 5. Complete viscoelastic model of central and peripheral arterial walls for a fixed smooth muscle contraction and small changes in ε_w.

In conclusion, central arterial viscosity is smaller than that in peripheral arterial model. The exemplary experimental data indicating that experimental elastic modulus magnitudes indeed have little frequency dependence for central arteries but not peripheral arteries [80].

Skin Tissue Viscoelastic Model

In this part, an appropriate model for the viscoelastic properties of skin tissue will be studied [81, 82, 83, 84]. In general, human skin consists of two main structures: the epidermis and the dermis. The epidermis which is the outer layer of the skin is mostly made up of flat, squamous cells, and basal cells. The dermis is the inner layer of skin and consists mainly of a complicated network of blood and lymph vessels, hair follicles, glands, nerve endings, and even small hair muscles.

The viscoelastic properties of the skin tissue has been studies over decades, one of the most popular models is based on the viscoelastic property which is associated in mechanics with combination of spring and dampers in different connection schema [81].
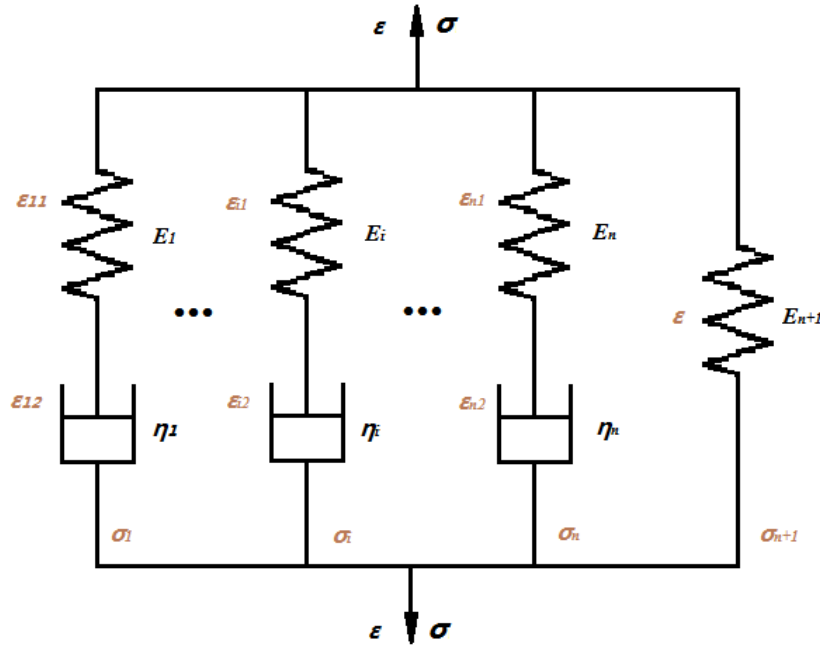

Figure 6. The modified Maxwell viscoelastic model of skin.

The viscoelastic models can be composed of discrete elastic and viscous components [82]. Maxwell and Kelvin model are the basic models of viscoelasticity [83]. Maxwell is a series connection of a spring and a damper as previously described, and Kelvin consists of parallel connected spring and damper connected in parallel. Based on the basic models, other more complicated models can be established, for example, generalized Maxwell model, Burgers model,

etc.

The existence of skin viscoelastic behavior had been verified by many experimental results [84, 85]. Referring to generalized Maxwell model, the viscoelastic constitutive model of the skin is established, which consists of Maxwell model in parallel. Because there is a series damper in each Maxwell model, the internal stress of material would become near to zero if the time of external load is longer enough. Therefore, in order to describe the material properties more accurately, an elastic element is connected in parallel with the generalized Maxwell model, as shown in Figure 15. We define the model as modified Maxwell viscoelastic model of the skin. The solid property, shown by the paralleled elastic element, which is denoted as E, reflects the residual stress of skin in the relaxation curves. The stress σ and strain ε of viscoelastic model in Figure 15 can be described as the equation:

$$\sigma = \sum_{i=1}^{n+1} \sigma_i \quad (20)$$

$$\varepsilon = \varepsilon_{i1} + \varepsilon_{i2}, \quad (i = 1, 2, \text{K } i, \text{K }, n) \quad (21)$$

where σ_i denotes the stress in the i-th sub-Maxwell model; ε_{i1} and ε_{i2} respectively denotes the strain of the i-th elastic and viscous component. Based on the equation (20) and (21), the constitutive equation of generalized Maxwell model is expressed as:

$$\sum_{i=1}^{n} \sigma_i + \sum_{i=1}^{n} \frac{\eta_i}{E_i} \sigma_i = \sum_{i=1}^{n} \eta_i \varepsilon_i \quad (22)$$

By applying to Laplace transform, the constitutive equation in transformed Laplace domain is given by:

$$\bar{\sigma} = \sum_{i=1}^{n} \left[\frac{\eta_i s}{1 + (\eta_i / E_i) s} \right] \cdot \bar{\varepsilon} = \sum_{i=1}^{n} \left[\frac{\eta_i s}{1 + \tau_i s} \right] \cdot \bar{\varepsilon} \quad (23)$$

where $\tau_i = \eta_i / E_i$. The differential equation is solved by Unit Step Function $\varepsilon = H(t)$ at a certain temperature, and stress response can be expressed as:

$$E(t) = \sum_{i=1}^{n} E_i e^{-t/\tau_i} \quad (24)$$

where τ_i is relaxation time of the i-th Maxwel model. Therefore, skin viscoelastic model shown in

the Figure 15 can be defined as:

$$E(t) = \sum_{i=1}^{n} E_i e^{-t/\tau_i} + E_{n+1} \quad (25)$$

The analytical form of the above equation is consistent with the generalized Prony-series model where E_i and τ_i are the model parameters; n is the number of Prony-series; E_{n+1} is the static elastic modulus (i.e., the long-term relaxation modulus).

The model can accurately describe material viscoelastic, and its parameters are also relatively easy to be obtained by numerical fitting based on stress relaxation tests.

Prototype Design

With the foundations of previously studied theories and models, the portable laser speckle imaging system is proposed and can be achieved by using innovative configurations with respect to electronic hardware and image processing algorithm.

As mentioned previously, laser speckle is a random self-interference pattern which is produced due to the roughness of the back reflecting surface and can be considered as a reference to track the changes in the phase of the light being scattered from the object's surface. The laser will illuminate the region of interest where the measurement is to be performed. The pattern is generated on the detector of the camera which is defocused by the aspheric lens after laser light is reflected from the illuminated surface. By properly adjusting the optical configurations of the camera, the tilting of the inspected back-reflecting surface will cause movements in the speckle pattern distribution. Therefore, the temporal shifts and movements of this random pattern can be tracked by performing proper correlation operations in software algorithms.

In this chapter, both hardware and software of the experimental configurations will be discussed and explained.

Hardware instruments

Images acquisition module

The image acquisition module consists of a laser diode and a complementary metal-oxide-semiconductor (CMOS) camera, aiming to capture the time-varying speckle pattern caused by pulsation of the laser illuminated radial artery. The lightweight setup could make the laser speckle imaging system more portable in order to increase access to the technology for health care applications. The technical configurations of the laser diode and CMOS camera will be discussed specifically.

Laser Diode

A laser diode is a semiconductor device that produces coherent radiation, in which the waves are all at the same frequency and phase, in the visible or infrared spectrum when electrical current passes through the semiconductor. Laser diodes only require lower power, thus it can operate using small battery power supplies but generate low intensity.
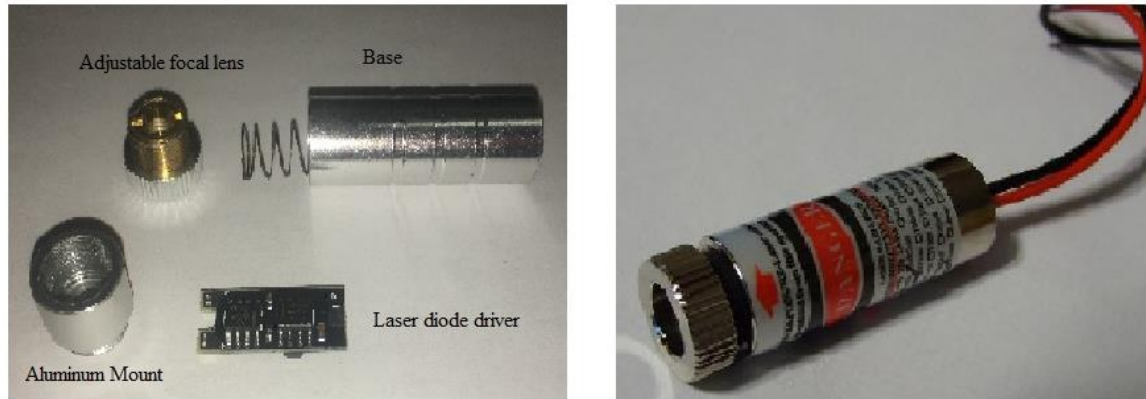

Figure 7. Diode laser module (right) and its configuration (left).

In order to reduce the side effects of the diode laser light such as skin and retina burn, a low output power laser with 650 *nm* wavelength (AixiZ, 5 *mW*) is used to illuminate the region of measurement, and the diode laser module is presented as Figure 17. An adaptable multi-focal glass lens is mounted along the laser diode to expand laser beam. The laser diode module is driven by a tunable circuit board, and is operating at the maximum 3.7 *V* and 35 *mA* in direct current.

CMOS camera module

Laser speckle imaging techniques utilize a simple instrumentation to perform non-contact vibration measurement. The digital camera module consists of a camera for detection of the backscattered light, and imaging optics to defocus the camera to image the near-field light plate onto the camera sensor. Digital camera have become extremely common as the prices have come down, and one of the drivers behind the falling prices has been the introduction of CMOS image sensor. In terms of the manufacture, a charge-coupled device (CCD) sensors are much more expensive than CMOS sensors. Both CMOS and CCD image sensors convert light into electrons

with its two dimensional arrays of photo detector, but they are different in the technology which reads the accumulated charge value of each sensor in the image. For a CCD device, the charge is transported across the chip and read at one corner of the array, then an analog-to-digital converter turns each pixel's value into digital value. In most CMOS sensors, transistors are connected with each pixel that amplify and move the charge individually. CCD sensors create high-quality, low-noise images while CMOS sensors consumes little power and are more susceptible to noise but much more inexpensive.

Net price	$25
Weight	3 g
Still resolution	8 Megapixels
Video modes	1080p30, 720p60 and 640$\times$480p60/90
Sensor	Sony IMX219
Sensor resolution	3280$\times$2464 pixels
Sensor image area	3.68 $mm$$\times$2.76 mm
Pixel size	1.12 $\mu m$$\times$1.12 μm
Optical size	1/4″
Focal length	3.04 mm
Focal ratio (F-stop)	2.00

Table 1. Hardware specification of Raspberry Pi® V2 camera module [102].

There are wide variations in the component specifications used for laser speckle imaging techniques worldwide and the digital cameras used in the studies vary from cost-effective CMOS sensors [94, 95] to expensive CCD [96, 97, 98]. But there are not enough pervasive evidences provided for the camera choice. Researches are focusing on reducing the cost of imaging methods but improving imaging performance for both laboratory research and clinical applications.

Scientific studies have evaluated the possibility of using CMOS devices to perform laser speckle imaging for medical applications in tracking movement of an artificial eye and skin movement [99], moreover the non-medical applications such as monitoring wood deformation and membrane vibration [100]. A low-cost CMOS camera sensors and low power laser sources were used in these studies, rather than the CCD camera which costs thousands of dollars. Moreover, the relative vibration profile calculated by the CMOS camera had significant agreement with those measured with the CCD camera [101]. Inspired by the previous studies, an inexpensive instrumentation consisting of a CMOS sensor camera and aspheric lens will be used for laser speckle imaging as camera module in this project.

For the image acquisition system in this project, the camera will be used is a Raspberry Pi® Megapixel V2 Camera Module, with Sony IMX219 CMOS sensor. The hardware specification is of the camera module V2 is presented in the Table 1 below.

In this part, the primary camera settings will also be discussed: aperture, exposure time or shutter speed, ISO, and focal length. Obviously there are indeed consideration regarding choosing the optimal parameters of the settings for good performance of further imaging analysis [93].
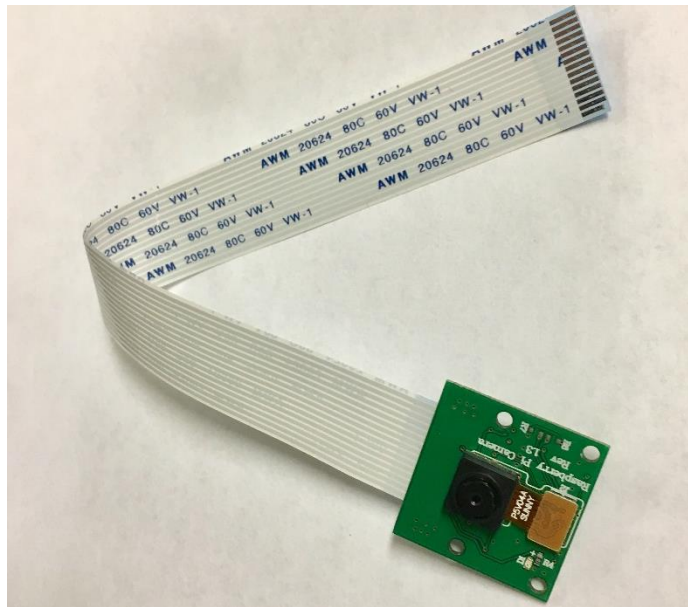

Figure 8. Raspberry Pi® 2V camera module.

Exposure time is the length of time when the digital sensor inside the camera is exposed to external light. The more photons captured by the sensors, the more those sensors increment their

18

counters. Raspberry Pi[®] 2V camera, like other mobile camera, has no physical shutter, thus light falling on the sensors and incrementing the counts cannot be prevented. In fact two steps are performed on the sensors for imaging: reset a row of sensors, and read a row of sensors. There are naturally limits to the minimum exposure time due to the fact of reading out a line of sensors must take a certain minimum time. In other words, maximizing the exposure time can be achieved to choose as little framerate as possible. Therefore the maximum exposure time is determined by the camera's minimum framerate. Exposure time of the camera also serves as a significance role on image blurring which is caused by movement of the object. According to a scientific research, the sensitivity and noise incorporation of laser speckle contrast imaging technology for blood flow changes measurement in rodent with a varying effective camera exposure values have been experimented. It concluded that the sensitivity to relative variations in speckle will increase with exposure time increases, and relative noise is also reinforced. In order to achieve good performance of laser speckle imaging, the studies have recommended that exposure time or shutter speed approximately 10 *ms* will maintain a good contrast to noise ratio [103].

The aperture is a physical property of the lens of the camera and the Raspberry Pi[®] V2 camera module has a fixed aperture of *f/*2.8. The size of speckle on the imaging plane totally depends on the camera optical configurations and its size of the speckle can be calculated by:

$$d = 1.22\lambda\left(f/\#\right)M \quad (55)$$

where *M* is the magnification of the optical lens, *λ* is the wavelength of laser light and *f/#* is the f-number of the camera module [104, 105]. In order to fulfil better statistical conditions for further image analysis, the speckle size has to be same with the pixel size of the image sensor. Note that the camera module is mounted with two replicated aspheric lenses (Edmund Optics, 68-118) which have a 10 *mm* diameter and 40 *mm* effective focal length to defocus the camera to a near-filed speckle plane. Moreover, these two tandem lens configuration make 1:1 imaging as well. The specifications of the replicated aspheric lenses are presented in Table 2. The *f/#* of the imaging system was calculated to be 4.4, while focal length equals to 40 *mm* and the aperture diameter of the image system equals to 9 *mm*. It is important to note that the speckle size should be approximately equals to the size of individual pixels, which is 1.12 *μm*. Apply to the Equation 45, the speckle size can be derived as 1.58 *μm*, which is approximately 1.41 pixels for the CMOS

camera module setup using an *f/#* of 2 and considering the magnification is 1.

Target Price	$19.95
Numerical aperture	0.11
Diameter	10 *mm*
Effective focal length	40 *mm*
Clear aperture	9 *mm*
Focal length specification wavelength	650 *nm*
f/#	3.85
Wavelength range	470 – 690 *nm*
Substrate	N-SF5

Table 2. Specifications of replicated aspheric lenses, manufactured by Edmund Optics.

The other important factor influencing sensor imaging is the sensor's gain, or known as ISO. ISO value evaluates the level of sensitivity of the camera to available light condition. The lower the ISO value, the less sensitive it is to the light; in other words, a higher ISO value will increase the sensitivity of the camera. With an increased sensitivity, camera sensor can capture images under low-light circumstances without using a flash. But the extra grain or noise to the pictures can be result from a higher sensitivity. With the Raspberry Pi® V2 camera module, ISO 60 produces overall gain of 1.0, ISO 100 produces an overall gain of 1.84, and ISO 800 of 14.72. In this project, ISO was set to 400 for the CMOS camera according to a study related to laser speckle imaging [106].

Images processing module

The imaging processing module employed for this project is a credit card size computer named with Raspberry Pi®. The Raspberry Pi® is a single computer board with small size and it can be used for many tasks like common computers. It was proposed and manufactured by the

Raspberry pi foundation from the United Kingdom. The Raspberry Pi® board is a portable device with a consumer-grade cost. The Raspberry Pi® comes with a set of open source technologies, which encouraged technologist to share and develop their scientific projects.

A Raspberry Pi® 3 board was used in this project and its full architecture consists of a program random-access memory (RAM), a central processing unit (CPU) and graphics processing unit (GPU), Ethernet port, and various interfaces for external devices such as CSI camera, HDMI video device and so on. The mass storage was designed to use a SD flash memory card, hence the Raspberry Pi® board will boot from this SD card with the operation system installed. The Raspberry Pi® board image processing module is depicted in Figure 19.
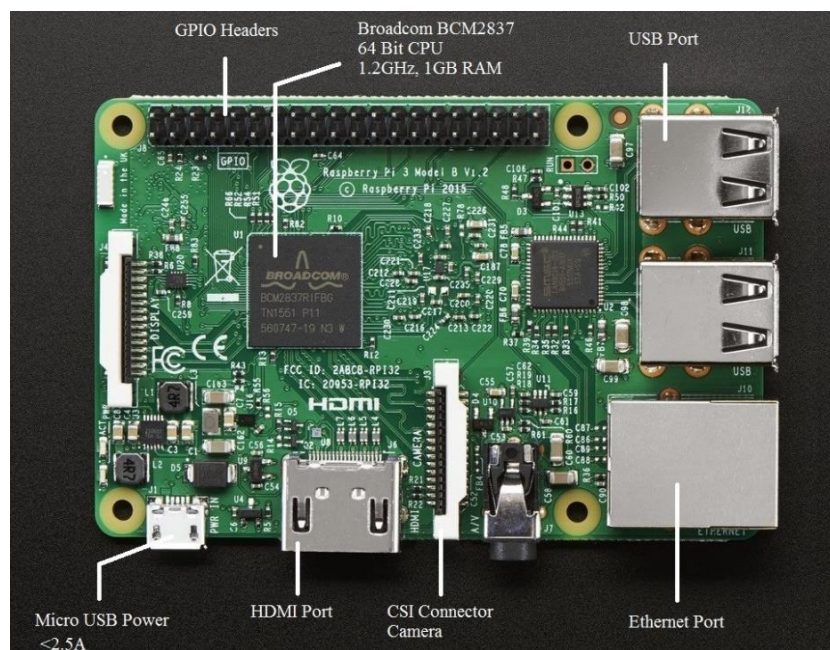

Figure 9. Raspberry Pi® 3 Model B.

CPU is responsible for carrying out the instructions of the computer through logical and mathematical operations while GPU is a specialized chip designed to speed up the operation of image or matrix calculations. CPU along with the GPU was integrated into a system-on-a-chip (SoC) Broadcom BCM2837. The CPU of Raspberry Pi® 3 equipped is a 64-bit quad-core clocked at 1.2 GHz with ARMv8 architecture and its GPU was designed with a Broadcom VideoCore IV which runs at 400 MHz. This kind of GPU core supports OpenGL ES 2.0, hardware-accelerated OpenVG, Open EGL, OpenMAX and 1080p30 H.264 high-profile decode. The Raspberry Pi® 3 board is designed with a 1024 M-byte of synchronous dynamic random access memory

(SDRAM). The specifications of the Raspberry Pi® 3 is listed in the Table 3.

It is necessary to mention that Raspberry Pi® 3 establishes a Debian-based computer operating system. It has been officially provided by the Raspberry Pi® Foundation as the primary operating system for Raspberry Pi® single-board computers.

Target Price	$35
System-on-a-chip	Broadcom BCM2837
CPU	1.2 GHz 64-bit Quad-core ARMv8 Cortex-A53 architecture
GPU	400 MHz Broadcom VideoCore IV, OpenGL ES 2.0,OpenVG 1080p60 H.264 high-profile encode and decode
Memory (SDRAM)	1024 M-Byte
Video ports	4 of USB 2.0
Onboard storage	MicroSD slot
Low-level peripherals	40 General Purpose Input/Output pins (GPIO), Peripheral interface bus, Universal asynchronous receiver/transmitter (UART)
Power source	5 V (DC) via Micro USB or GPIO header

Table 3. Specifications of Raspberry Pi® 3 board.

Software design

Inspired by the previously described mathematic model, the temporal shifts of back-reflected laser speckle pattern can be tracked by applying a correlation operations in software algorithms, which allowed us to determine the magnitude of the subject's local surface displacement. A

preprocessing procedure is applied to extract Region of Interest (ROI) before the correlation based algorithm. By analyzing the displacement profile caused by pulse pressure, the heart rate and radial augmentation index can be measured. The images processing algorithm are realized via Matlab[®] and Python software codes.

Images preprocessing

Image preprocessing is necessary to achieve an optimal conditions for further analysis. In this procedure, tracking ROI in order to reduce the extra size of the image will be achieved by satisfying the statistics property of the speckle pattern. The images preprocessing procedures were designed to capture the frames, and extracted the ROI of speckle pattern by controlling an optimization condition. The purpose of extracting the ROI to analyze is reduce the data size in order to accelerate the processing time per frame. Even though the imaging processing module of Raspberry Pi[®] employed an efficient GPU to do the graphic operation such as matrix calculation, once the resolution of the frame reaches to a thousand scale, the time complexity for single frame operation increases; thus the time consume of the software will increase dramatically. Another problem should be overcame is the artifacts of the mobile device and it will fail to fully detect the speckle pattern in ROI. Thus, design an algorithm to reduce the artifact and narrow down the ROI can provide benefits for the efficiency of the algorithm.

Regarding to the statistics of laser speckle, the field associated with a singly linear polarization will be complex and circular Gaussian if the illuminated surface is rough enough with respect to the laser wavelength. The laser speckle intensity, *I*, obeys a negative exponential distribution and the intensity probability varying between *I* and *I+dI* as described [107]:

$$p(I \mid I_m) = \begin{cases} \left(\dfrac{1}{I}\right) e^{-\frac{1}{I}} & I \geq 0 \\ 0 & I < 0 \end{cases} \quad (45)$$

I_m denotes a mean intensity. With the property of the negative exponential, the distribution of the intensity has a long tail compared with a standard Gaussian distribution. Under the distributing condition for detecting the speckle pattern, a statistical parameter of a speckle intensity distribution was designed to satisfy $I_a/I_d > 0.2$, wherein I_a is the mean value of the speckle intensity
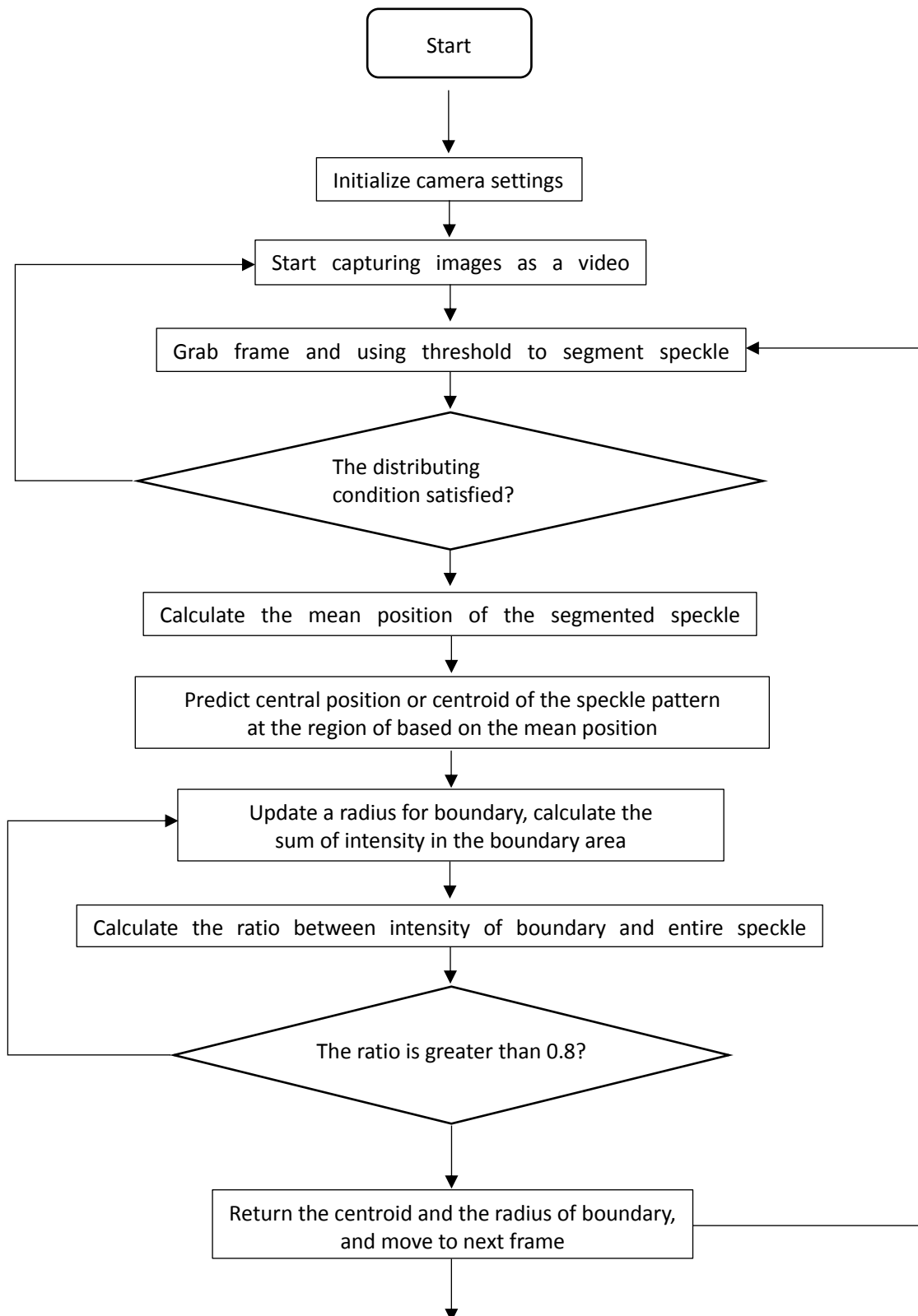
in ROI and

Figure 20. The flow diagram of the algorithm for image preprocessing.

I_d is the maximum value of a detected speckle intensity. For algorithm implementation, the distributing condition is designed to be a feedback signal and controls the output power of a subsequent laser light source. The frame are transferred for further processing once the distributing condition is satisfied. By satisfied the preprocessing, the speckle pattern can be stabilized in real time.

In order to extract speckle pattern, the size of the detected speckle pattern should be controlled by estimate a center of the detected speckle pattern using:

$$x_c = \sum_{i=1}^{n} x_i I_i(x, y) \Bigg/ \sum_{i=1}^{n} I_i(x, y) \quad (46)$$

$$y_c = \sum_{i=1}^{n} y_i I_i(x, y) \Bigg/ \sum_{i=1}^{n} I_i(x, y) \quad (47)$$

where x_c and y_c are coordinates of the center of the detected speckle pattern, also known as centroid. x and y are the coordinates in the detector surface, n is a total number of the pixels in the detector surface, and I denotes a value of the light intensity. Once the centroid of the detected laser speckle pattern is determined, an iteration operation is perform to fulfill a statistically condition for determining the boundary of the ROI, wherein this boundary of the ROI corresponds to 80% of the detected light intensity. The flow diagram of the preprocessing procedure is presented in Figure 20.

Correlation based algorithm

The processing module calculates the correlation of the captured time-varying speckle pattern to determine a difference of the current shape of the pulse waveform. The images are compared by performing a correlation based technique in which the phase peak shift of the correlation between two consecutive images are calculated. The shift in a correlation peak location in the correlation profile is defined as the pixel shift, and such shift reassemble single samples on the vibration profile of the object's surface [108]. The correlation between two signals, which also named as cross correlation, is a standard method for feature detection and it is also performed to estimate the degree to which two series or matrices are correlated.

For illustrating the mathematical idea of cross correlation, firstly take two series $x(i)$ and $y(i)$ rather than two dimensional matrices for consideration, where $i=0, 1, 2 \ldots N\text{-}1$. The cross correlation r at delay d is defined as:

$$r(d) = \frac{\sum_i \left[\left(x(i) - m_x \right) * \left(y(i-d) - m_y \right) \right]}{\sqrt{\sum_i \left(x(i) - m_x \right)^2} \sqrt{\sum_i \left(y(i-d) - m_y \right)^2}} \quad (46)$$

where m_x and m_y are the means of the corresponding series. When the index of the series is less than zero or greater than or equal to the number of points, such as $i\text{-}d < 0$ and $i\text{-}d \geq N$, the commonly used approaches are to either ignore these points or assume the x and y equal to zero for $i < 0$ and $i \geq N$. In signal processing applications, the series are considered to be circular so that the range indexes are wrapped back at the beginning and the end, for example $x(-1) = x(N\text{-}1)$, $x(N+5) = x(5)$. The denominator in the Equation 46 above performs as a normalization for correlation coefficients such that $-1 \leq r(d) \leq 1$, where bounds indicate the maximum correlation and zero indicates no correlation. A high negative correlation indicates a high correlation but of the inverse of one of the series.

The textbook presentations of correlation describe the convolution approaches. Due to the computational cost of spatial domain convolution, a faster algorithm is therefore of interest. There are several fast convolution algorithms that do not use transform domain computation [109]. The attendant possibility of efficiently computing correlation in the frequency domain using the fast Fourier transform, due to the complex convolution operations is then multiplications, real additions and subtractions. Phase correlation is a more robust method and uses frequency domain method which is based on the Fourier shift property of Fourier transform. It is a subset of cross correlation techniques. In this algorithm, the transform coefficients are normalized to the magnitude before computing correlation in the frequency domain. Therefore, the correlation is only dependent on phase information and is less sensitive to the changes in image intensity.

In this project, the peak shift laser speckle pattern is calculated through phase correlations between the ROI of frames and the implementation of phase correlation will give the estimation of translational motion of the object. Phase correlation performs transform domain computation and employs the Fourier shift properties of Fourier transform.

The algorithm is designed by firstly applying a windowing technique to each preprocessed frame in order to remove possible edge effect, and Hanning window is employed in this project. Consider two consecutive processed images $g_a(x, y)$ and $g_b(x, y)$ in the time series. Then calculate two dimensional forward discrete Fourier transform $G_a(u, v)$ and $G_b(u, v)$:

$$G_a[u,v] = \sum_{m=0}^{M-1}\sum_{n=0}^{N-1} g_a[m,n] \cdot e^{-j2\pi(\frac{u}{M}m+\frac{v}{N}n)} \quad (47)$$

$$G_b[u,v] = \sum_{m=0}^{M-1}\sum_{n=0}^{N-1} g_b[m,n] \cdot e^{-j2\pi(\frac{u}{M}m+\frac{v}{N}n)} \quad (48)$$

where M, N denotes the size of the image. Cross Power Spectrum is calculated as following:

$$R = \frac{G_a[u,v] \cdot G_b[u,v]^*}{\left| G_a[u,v] \cdot G_b[u,v]^* \right|} \quad (49)$$

Next the cross-correlation is converted back into the time domain via the inverse discrete Fourier transform:

$$r[x,y] = \sum_{k=0}^{M-1}\sum_{l=0}^{N-1} R[k,l] \cdot e^{j2\pi\left(\frac{k}{M}m+\frac{l}{N}n\right)} \quad (50)$$

Finally, it computes the peak location in $r[x, y]$:

$$(\Delta x, \Delta y) = \arg\max_{(x,y)}(r) \quad (51)$$

The flow diagram of the correlation based algorithm procedure is presented in Figure 21.

Waveform analysis

By the phase correlation algorithm, the peak shifts of cross correlation are derived. As the previously studied theories, the peak shift indicates the vibration profile which related to pulse waveform. Therefore the cardiovascular parameters such as heart rate, and radial augmentation index can be measured by waveform analysis. The waveform analysis algorithm is based on the peak detection techniques, because the peaks and inflections in the waveform indicate the significant features caused by hemodynamic activities [63]. For example, the radial augmentation index is defined as the ratio between first and second systolic peak with respect to diastolic value,

27

and it can be utilized to quantify the arterial stiffness and evaluate the cardiovascular risk.
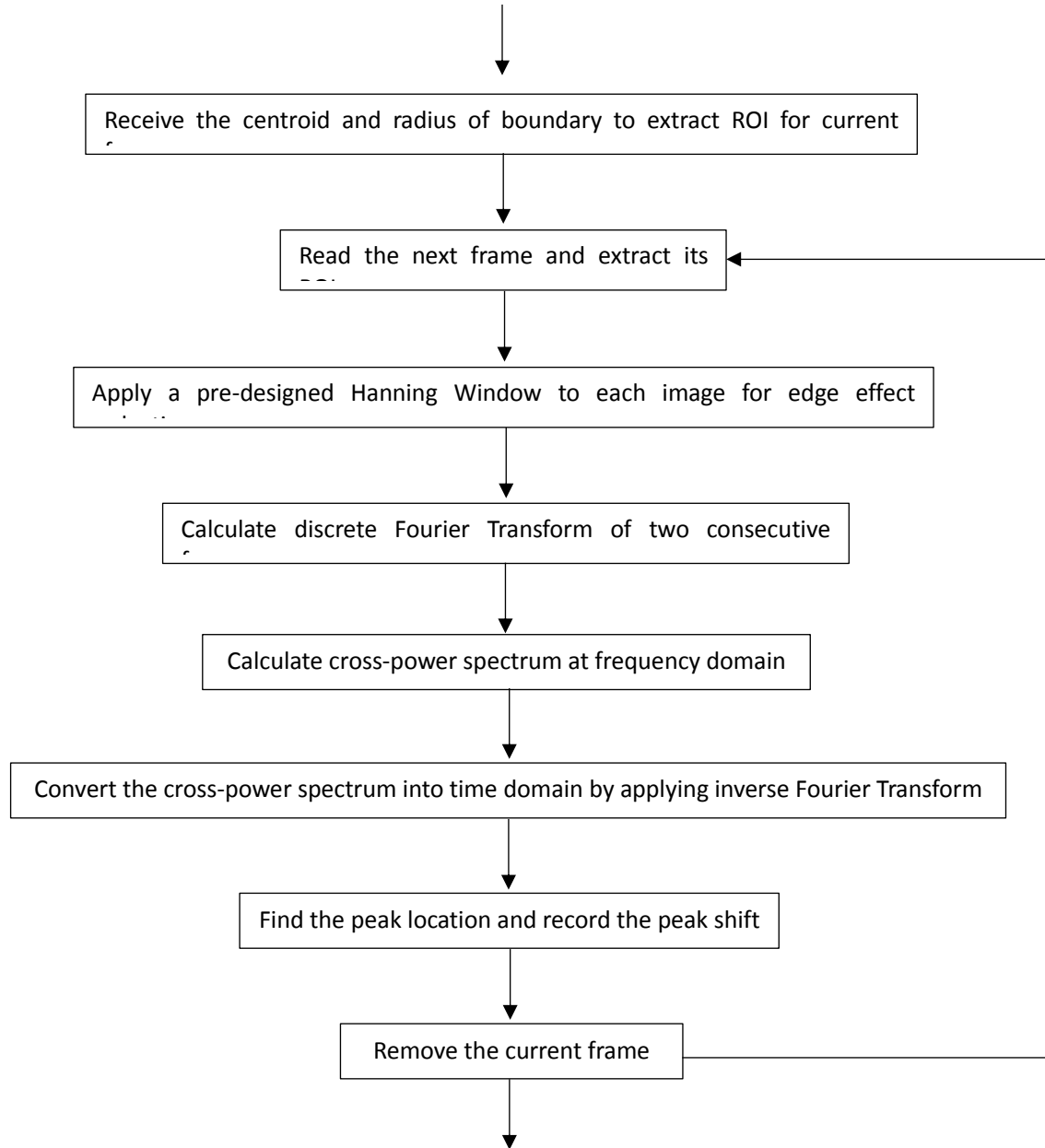
Receive the centroid and radius of boundary to extract ROI for current

Read the next frame and extract its

Apply a pre-designed Hanning Window to each image for edge effect

Calculate discrete Fourier Transform of two consecutive

Calculate cross-power spectrum at frequency domain

Convert the cross-power spectrum into time domain by applying inverse Fourier Transform

Find the peak location and record the peak shift

Remove the current frame

Figure 21. The flow diagram of the correlation based algorithm.

The waveform analysis firstly involved correlation of the time-varied speckle patterns and plotting the amplitude of the relative shift of the correlation peak over time. The derivative based peak detection method amplifies the high frequency component of noises. Thus, initial smoothing

and filtering of the raw data is necessary to eliminate the high frequency noise in the waveform. Then set a value for the window size in order to eliminate the repetitively detected peaks. A sliding window is applied to the waveform, and use the peak detection algorithm at every window. Moreover, the window size is changed for detecting second systolic peaks and remove the repetitive detection. At last step, the obtained data from waveform are used to calculate and display the cardiovascular parameters such as heart rate and radial augmentation index. The flow diagram of the waveform analysis algorithm is presented in Figure 22.
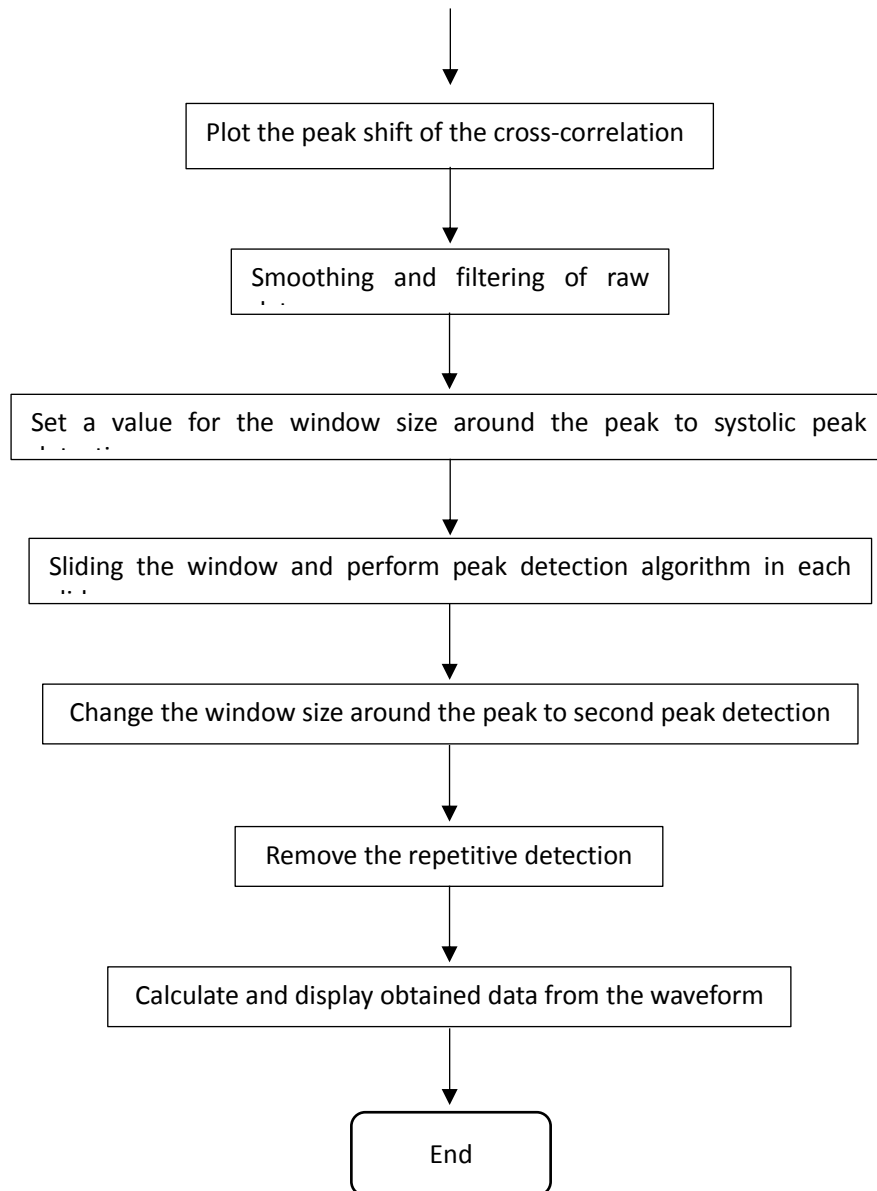

Figure 22. The flow diagram of the waveform analysis algorithm.

Experiment Setup

Inspired by the previously described mathematic model, the temporal shifts of back-reflected laser speckle pattern can be tracked.

In terms of the entire experiments setup of this project, it is not complicated. The visible diode laser source at 650 *nm* wavelength and low power 5 *mW* illuminates the region of interest where the measurement should be performed. For this project, the measurement is chosen to be performed at the surface of the wrist where the radial artery locates beneath. Speckles are reflected from the illuminated surface and the speckle pattern is projected on the detector of the camera sensors. The reflected speckle pattern from the wrist of the subject is captured by a CMOS camera with pixel size 1.12 *μm* $\times$ 1.12 *μm* connected to a computer. The optics of the camera is slightly defocused by a tandem of aspheric lenses in order to make same size of the speckle as that in pixels, while this feature of the configuration is such important to convert the tilting movement of the object's inspected surface into the related peak shift in correlation of the speckles. This is a significant property that makes the speckle pattern be constant under deformation varying of the inspected object with laser illumination, and also distinguishes this phenomenon from other laser speckle-related techniques where the pattern varies in a non-controllable situation. The constructed system is presented in Figure 23, where a sketch of the system presents on the left, and the real configuration on the right.

The focal length of the tandem configuration of optics are 4 *mm* and the distance from the laser emitter to the subject's wrist is about 30 *cm*. In all of our experiments, the frame rate of the camera was set to 45 *fps*, the resolution was 1296 $\times$ 730. In order to obtain good quality of the laser speckle imaging, the ISO was chose to be 400, brightness was 30, shutter speed or exposure time was set to 10 *ms*. Incidence angle of the laser beam was set to be 90 degree with respect to the subject's wrist to obtain the smallest beam spot size. Therefore, the size of the speckle obtained on the camera was at the largest possible size at the given distance from camera. Generally, the speckle spot size is linearly to the distance between the camera device and the object, and inversely proportional to the diameter of that laser beam spot.
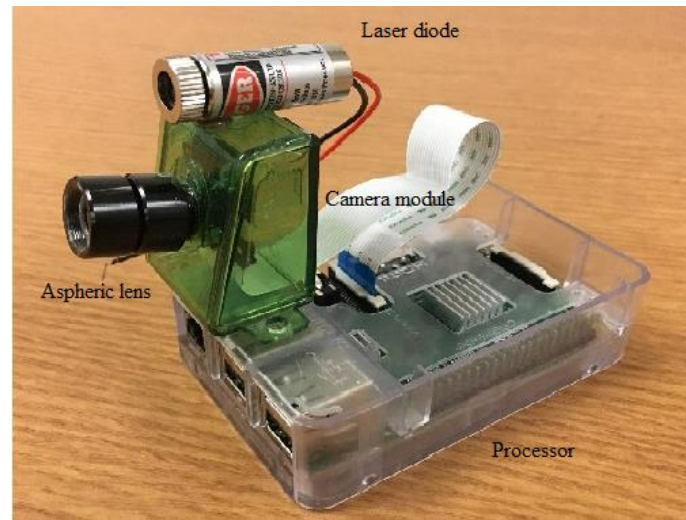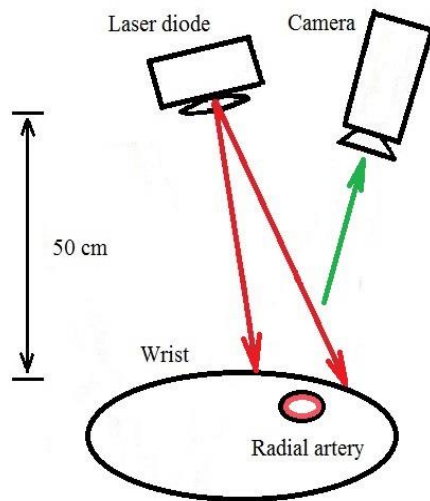
Figure 23. Implemented experimental configuration for non-invasive system. (Left is sketch of the measurement system; Right is real configuration of the prototype).
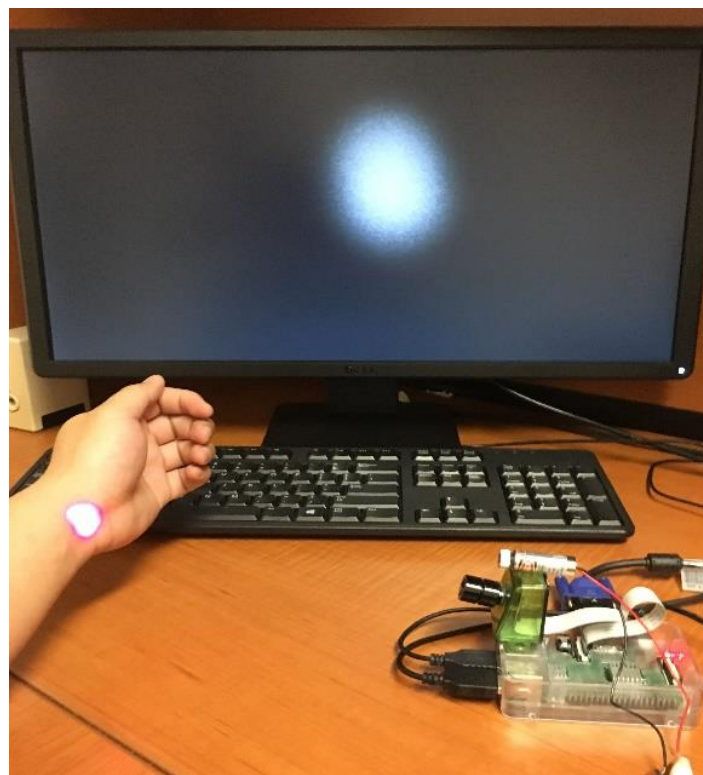

Figure 24. Non-contact measurement of pulse pressure waveform experiment.

The camera captured the frames with laser speckle pattern and the frames were sent to the processing module to be further analyzed by predesigned algorithms. By applying preprocessing,

correlation based algorithm, the measurement involved correlation of the time-varied speckle patterns and plot the magnitude of the relative peak shifts of the correlation over time. The image processing algorithms is firstly realized via m-language on the Matlab® platform (the MathWorks, Inc., United States) for evaluating the performance and analyzing results. These algorithms were transferred and execute onto the Raspberry Pi® platform by rewriting these algorithms with Python programming language. The software system aims to derive the pulse waveform of the examiner, moreover, the heart rate and radial augmentation index can be extracted via the further pulse waveform analysis.

(a)   (b)

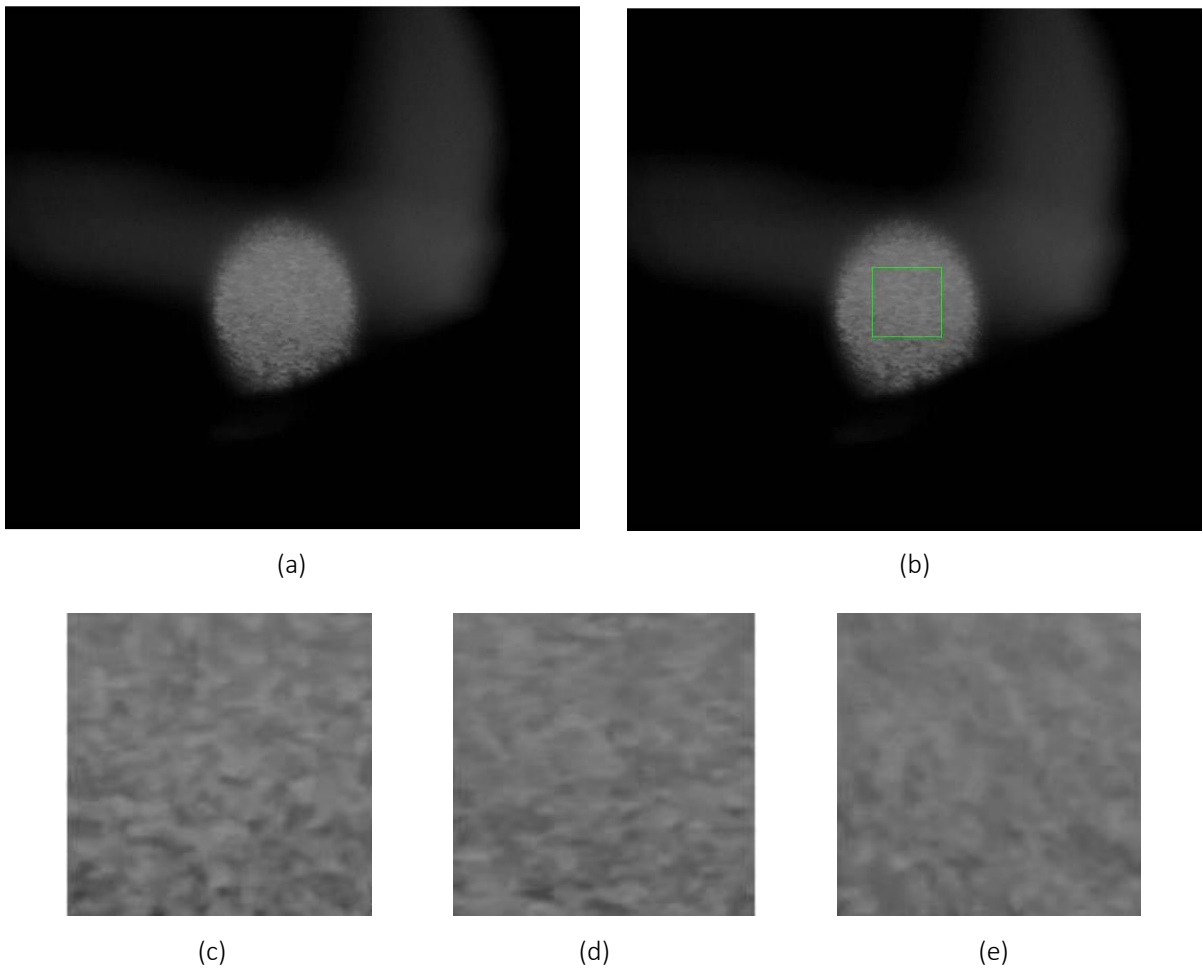(c)   (d)   (e)

Figure 25. Frames captured by camera. (a) shows the captured laser speckle during experiment. (b) applied preprocessing algorithm to detect ROI; (c) (d) (e) are three consecutive ROI of frames obtained.